Journal of Soils and Sediments (2024) 24:2132–2143
https://doi.org/10.1007/s11368-024-03767-0

SEDIMENTS, SEC 2 • PHYSICAL AND BIOGEOCHEMICAL PROCESSES • RESEARCH ARTICLE

Computationally characterizing the diffusive boundary layer in lakes and reservoirs

Xiamei Man[1] · Chengwang Lei[2] · Kevin A. Bierlein[3] · Lee D. Bryant[4] · Abigail S. Lewis[5] · Cayelan C. Carey[5] · John C. Little[6]

Received: 24 September 2023 / Accepted: 27 February 2024 / Published online: 16 March 2024

Abstract

Purpose Hypolimnetic hypoxia has become increasingly prevalent in stratified water bodies in recent decades due to climate change. One primary sink of dissolved oxygen (DO) is sediment oxygen uptake (J_{O_2}). On the water side of the sediment–water interface (SWI), J_{O_2} is controlled by a diffusive boundary layer (DBL), a millimeter-scale layer where molecular diffusion is the primary transport mechanism. In previous studies, the DBL was determined by visual inspection, which is subjective and time-consuming.

Material and methods In this study, a computational procedure is proposed to determine the SWI and DBL objectively and automatically. The procedure was evaluated for more than 300 DO profiles in the sediment of three eutrophic water bodies spanning gradients of depth and surface area. Synthetic DO profiles were modeled based on sediment characteristics estimated by laboratory experiments. The procedure was further verified adopting the synthetic profiles.

Results and discussion The procedure, which was evaluated for both measured and synthetic DO profiles, determined the SWI and DBL well for both steady and non-steady state DO profiles. A negative relationship between DBL thickness and aeration rates was observed, which agrees with existing literatures.

Conclusions The procedure is recommended for future studies involving characterizing DBL to improve efficiency and consistency.

Keywords Sediment kinetics · Hypolimnetic oxygenation · Microprofiles · Dissolved oxygen · Sediment–water interface · Hypoxia

1 Introduction

Climate change is causing surface water temperatures to increase in many water bodies (both marine and freshwater), driving increased duration and intensity of summer stratification. Increased stratification can limit the transport of dissolved oxygen (DO) from surface to bottom waters, exacerbating hypoxia in stratified water bodies (Bryant et al. 2010; Jenny et al. 2016; Birt et al. 2021; Jane et al. 2021). Much attention has been drawn to sediment oxygen uptake (J_{O_2}) when managing or studying hypoxia in stratified water bodies, as J_{O_2} is the major sink of DO in hypolimnia. J_{O_2} also has important implications for biological activity, release of

Responsible editor: Hezhong Yuan

✉ Xiamei Man
x.man@uq.edu.au

[1] School of Civil Engineering, The University of Queensland, St Lucia, QLD 4072, Australia

[2] Centre for Wind, Waves and Water, School of Civil Engineering, The University of Sydney, Sydney, NSW 2006, Australia

[3] Hydros Consulting Inc, 1628 Walnut St, Boulder, CO 80302, USA

[4] Department of Architecture and Civil Engineering, University of Bath, Claverton Down, Bath BA2 7AY, England, UK

[5] Department of Biological Sciences, Virginia Tech, Blacksburg, VA 24061, USA

[6] Department of Civil and Environmental Engineering, Virginia Tech, 401 Durham Hall, Blacksburg, VA 24061, USA

nutrients from sediment, carbon cycling, and water-quality in water bodies, with microbial activity in upper sediments often being greater than in the water column (Glud 2008). Globally, the availability of DO in hypolimnia affects atmospheric oxygen, carbon dioxide (CO_2), and methane (CH_4) concentrations and thus has profound impacts on future climate (Berner and Canfield 1989; Archer and Maier-Reimer 1994).

Due to the negative consequences of hypolimnetic hypoxia, some lake and reservoir managers have implemented strategies to increase oxygen in hypolimnia, including hypolimnetic aeration and oxygenation systems (Ashley 1985) such as bubble plume diffusers (McGinnis and Little 2002) and airlift devices (Burris et al. 2002). These techniques have been shown to be effective for increasing hypolimnetic oxygen concentrations and suppressing the flux of reduced species out of sediment (e.g., iron and manganese) (Zaw and Chiswell 1999; Bryant et al. 2011a; Gerling et al. 2014) and have been verified in long-term case studies (Gantzer et al. 2019; Preece et al. 2019), but caution is needed when adding DO to the hypolimnion to avoid increasing sediment oxygen uptake (J_{O_2}), which can be induced by oxygenation itself (Gantzer et al. 2009; Bryant et al. 2011b).

J_{O_2}, the main oxygen sink in the hypolimnion of relatively shallow lakes and reservoirs (Nürnberg 1987), is usually modeled in hydrodynamic and water-quality models as a DO sink in the bottom of water bodies using literature or calibrated values, for example, in the commonly used lake model GLM-AED2 (Hipsey et al. 2019) or empirical expressions (Moore et al. 1996; Beutel 2003) when oxygenation systems are deployed.

J_{O_2} is influenced by both the complex oxygen consuming processes on the sediment side of the sediment–water interface (SWI) and the characteristics of the bottom boundary layer (BBL) on the water side of the SWI (see Fig. 1). The BBL is defined as the region of the water column directly affected by the SWI (Boudreau and Jørgensen 2001). The BBL comprises a turbulent boundary layer (TBL), a viscous sublayer, and a diffusive boundary layer (DBL), as shown in Fig. 1. In the TBL, ~ 1 m above the SWI, momentum transport is governed by turbulent eddies, and solutes are transported at a much faster rate than that by molecular diffusion (Boudreau and Jørgensen 2001). As the SWI is approached, turbulence gradually decreases until the vertical transport of momentum is governed primarily by molecular diffusion in the viscous sublayer (~ 1 cm above the SWI). Solute transport at the SWI is controlled by molecular diffusion in the DBL directly above the SWI, which is a millimeter-scale layer with a thickness governed by the turbulence in the BBL (Beutel 2003). In modeling practice, it is common to adopt a simplified two-layer BBL with the DBL immediately below the TBL (Brand et al. 2009; Bryant et al. 2010).

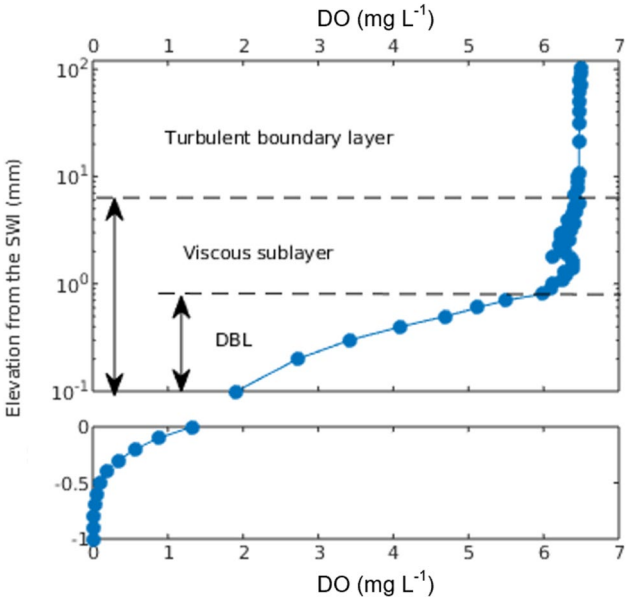

Fig. 1 A representative dissolved oxygen profile obtained in Carvins Cove Reservoir including the turbulent boundary layer, viscous sublayer, diffusive boundary layer (DBL), and the sediment–water interface (SWI). The upper bound of the viscous sublayer and diffusive boundary layer are indicated by dashed lines. For clarity, the dissolved oxygen profile is shown above the sediment–water interface in a log scale and below the sediment–water interface in a linear scale

On the sediment side of the SWI, J_{O_2} is influenced by various oxygen consuming processes including organic matter mineralization and chemical cycling within the upper sediment, as well as upward diffusing reduced chemical species from the deep sediment (Müller et al. 2012).

Efforts to understand sediment DO transport are often limited by the subjective and time-consuming characterization of the DBL thickness (δ_{DBL}). In the common "effective DBL" approach (Jørgensen and Revsbech 1985), δ_{DBL} is obtained by extrapolating the DO gradient from the SWI to the DO value of the bulk water. This widely adopted approach is practical because the DBL upper boundary may be ambiguous in some DO profiles. In this approach, the SWI is determined by visual inspection (Bryant et al. 2010; Bierlein et al. 2017; Man et al. 2020). However, in some circumstances, the DBL lower boundary (i.e., the SWI) may also be ambiguous, especially for permeable sediments and at high energy dissipation rates (Riedl et al. 1972). Bryant et al. (2010) compared the water-side and sediment-side approaches to evaluate J_{O_2} and δ_{DBL}, concluding that J_{O_2} and δ_{DBL} on both sides are influenced by the location of the SWI. Determining the SWI by visual inspection may be inaccurate and may adversely impact the quality of sediment/DBL modeling studies.

To overcome these challenges, a computational procedure is introduced in this study to determine the SWI and

the lower DBL boundary objectively and automatically. More than 300 DO profiles obtained in the laboratory and in situ are examined using both the visual inspection and computational methods. Previously, there have been some DO microprofile datasets (Hoffmann et al. 2020), but few of them include in situ freshwater DO microprofile studies. Laboratory microprofiling is much more cost-effective than in situ data collection, but without the ability to replicate the DBL, the laboratory microprofiling results are not comparable to in situ results. This study attempts to resolve this issue by creating a DBL in the laboratory by diffused aeration. In addition, modeled profiles referring to Brand et al. (2009) are also analyzed by the computational procedure to more conclusively validate the procedure.

2 Materials and methods

2.1 Study sites

The study sites are Falling Creek Reservoir (FCR) and Carvins Cove Reservoir (CCR), both in southwestern Virginia, USA, and Lake Hallwil (LH), located north of Lucerne in Switzerland. Table 1 provides the surface area, volume, maximum water depth, and elevation for the three study sites.

Falling Creek Reservoir (Chen et al. 2017) is a shallow, eutrophic reservoir which is equipped with a hypolimnetic oxygenation system. One sediment core was extracted in the shallow epilimnion of the reservoir on 9 November 2020. The sediment core was stored in a fridge set to 4 °C for 1 day and then placed in an ice-water bath during microprofile measurements.

Carvins Cove Reservoir (Bierlein et al. 2017) is the main drinking water supply for the Roanoke region, Virginia, USA. CCR is a relatively shallow and eutrophic reservoir, whose width and length are ~ 600 m and ~ 8000 m, respectively. Two parallel line-source diffusers located in the hypolimnion add oxygen employing a wide range of oxygen flow rates in the stratified period. Both FCR and CCR are managed by Western Virginia Water Authority.

Lake Hallwil (Bierlein et al. 2017) is a deep, medium-sized and eutrophic natural lake, which is 8.3 km long and 1.4 km wide. Six diffusers are arranged in a circle in the deepest region to add oxygen to the hypolimnion.

Seasonal anoxia occurs in LH while CCR maintains better DO level and hypolimnion anoxia only happens in summers (Holzner et al. 2012; Doubek et al. 2018). Both LH and CCR are dimictic, and the inflow conditions are weak. According to Wang et al. (2023), the first-order internal seiche mode in CCR and LH have a period of 10.5 h and 14 h, relatively. These internal motions lead to oscillating BBL but the BBL turbulence still shows quasi-steady structures given the long seiche time scales.

Table 1 Physical characteristics of the study sites

Water body	Surface area (km^2)	Volume (m^3)	Max depth (m)	Elevation (m above mean sea level)
FCR	0.12	32×10^5	9.3	507
CCR	2.5	24×10^6	22	357
LH	10	285×10^6	48	449

2.2 Microprofile measurements

A microprofiler (MP4; Unisense A/S) was used to measure oxygen microprofiles in the FCR sediment core in the laboratory (over a period of 4 days in 2020) and in situ (over a period of 5 days in CCR in 2013 and 4 days in LH in 2012). The microprofiler was equipped with a Clarke-type oxygen microsensor (Unisense OX-100) calibrated using the lower sediment as the zero reading and aerated water as the atmospheric reading. Microprofile measurements were made in triplicate at a sampling rate of 1 Hz. After estimating the location of the SWI, measurements were made at approximately the following vertical spatial resolutions: 10-mm resolution from 95 to 15 mm above the estimated SWI, 1-mm resolution from 14 to 5 mm above the SWI, and 0.1-mm resolution from 4.9 mm above the SWI to 5 mm below the SWI. The protocol measures a complete DO profile roughly every hour (Bierlein 2015).

2.3 Aeration/oxygenation schedule

At each study site, the aeration/oxygenation rate varied and the data collected at different aeration/oxygenation rates were analyzed to evaluate the performance of the computational procedure. Due to the inherent differences between the laboratory and in situ experiment setups, different terms are used to describe the DO addition into the water. "Aeration" is used for the FCR core where air is added using a bubbler in the laboratory sediment core, whereas "oxygenation" is used for CCR/LH, where concentrated oxygen gas is added and stratification is retained. Table 2 presents the aeration/oxygenation schedule for the three study sites. In the laboratory experiment, a mini-diffuser was used to add DO to the water, simulating a hypolimnetic aeration system in the field. The aeration rates (see Table 2) at FCR (core) were measured by an Alicat flow controller. The mini-diffuser (2 cm height, 1 cm diameter) was placed in the water above the sediment core at approximately 2 cm above the sediment. Figure 2 presents a schematic of the setup for the FCR laboratory experiment.

Table 2 Schedule of the laboratory and field (Rezvani 2016) campaigns

FCR (laboratory)	Hours	0–2	2–23		24–45		46–69	70–79	
	Aeration rate (slpm[a])	0	0.01		0.04		0.01	0	
CCR (in situ)	Hours	0–23	24–47		48–71		72–95	96–119	
	Oxygenation rate (slpm)	1104	789		473		237	0	
LH (in situ)	Hours	0–46		47–97		98–144		145–189	
	Distance (m)[b]	300		3700		30		30	
	Oxygenation rate (slpm)	2838						0	

[a]Standard liter of air at one atmospheric pressure per minute

[b]In LH, the measurements were carried out at different distances from the centrally located diffusers

2.4 The computational procedure

Figure 3 presents a typical DO profile with major components involved in the computational procedure (i.e., the fitted curve, SWI, gradient at the SWI, preliminary and final DBL upper bounds) identified in the profile. Figure 3a presents the entire DO profile from the measurement, and Fig. 3b presents the part of the DO profile closer to the SWI. The computational procedure applied to each DO profile to determine the SWI is:

I. First, the monotonic part of the DO profile curve (in Fig. 3b, 95.5–100 mm lander position) is characterized with a best-fit polynomial $x = f(\mathrm{DO})$ using MATLAB Curve Fitting Toolbox (The MathWorks Inc 2022) (the blue fit curve in Fig. 3b). The best-fit polynomial refers to the fit with the smallest least-square error.
II. The second derivative ($\frac{d^2x}{dDO^2}$) of the fitted curve is calculated to determine the SWI location and a preliminary DBL upper bound (the brown line in Fig. 3b) as the first and last points where the sign of the second derivative changes, respectively.

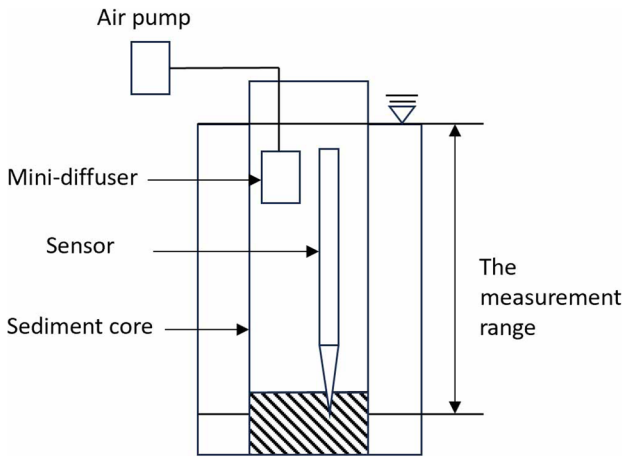

Fig. 2 The laboratory experiment setup used to measure microprofiles in the Falling Creek Reservoir sediment core

Regarding the order of the best-fit polynomial in the first step, a 4th order polynomial is the lowest order polynomial applicable to the computational procedure because the first and last points where the sign of the second derivative changes are used to identify the preliminary DBL bounds. If the second derivatives are of a linear relationship with the DO concentration (i.e., the best-fit polynomial is 2nd or 3rd order), there is only one point where the sign of the second derivative changes. After testing from 4 to 10th order polynomials, a 6th order polynomial was adopted in this study to ensure fitting accuracy (with $R^2 > 0.90$ for more than 90% profiles) and to avoid overfitting. Users of this computational procedure can easily adjust the polynomial order, or criteria/thresholds based on their experimental conditions and requirements. For DO profiles at steady state, users may start with the 4th order polynomials, and for DO profiles with noisy signal or at non-steady state, the 5th or 6th order polynomial is recommended.

When adopting a visual inspection method, the DO profile is examined carefully to determine the SWI as the point where the concentration gradient decreases due to the porosity difference between water and the sediment (Bryant et al. 2010; Man et al. 2020).

For both the computational and visual inspection methods, the upper bound of the DBL is characterized by the following steps:

I. The data points between the SWI and the preliminary DBL upper bound are used in an ordinary least squares regression to obtain the DO gradient ($\frac{\partial C}{\partial x}$) (the black line in Fig. 3b) in the DBL region.
II. The final DBL upper bound is determined by extrapolating $\frac{\partial C}{\partial x}$ to the DO concentration in bulk water (C_{bulk}) of the water column (indicated by the cyan line in Fig. 3a and b), which is calculated as the average DO concentration of the first nine measurements (that is, the first nine data points from the top in Fig. 3a). These nine measurements correspond to 15 mm to 95 mm lander positions with a 10-mm interval.
III. The δ_{DBL} is then determined as the distance between the SWI and the final DBL upper bound.

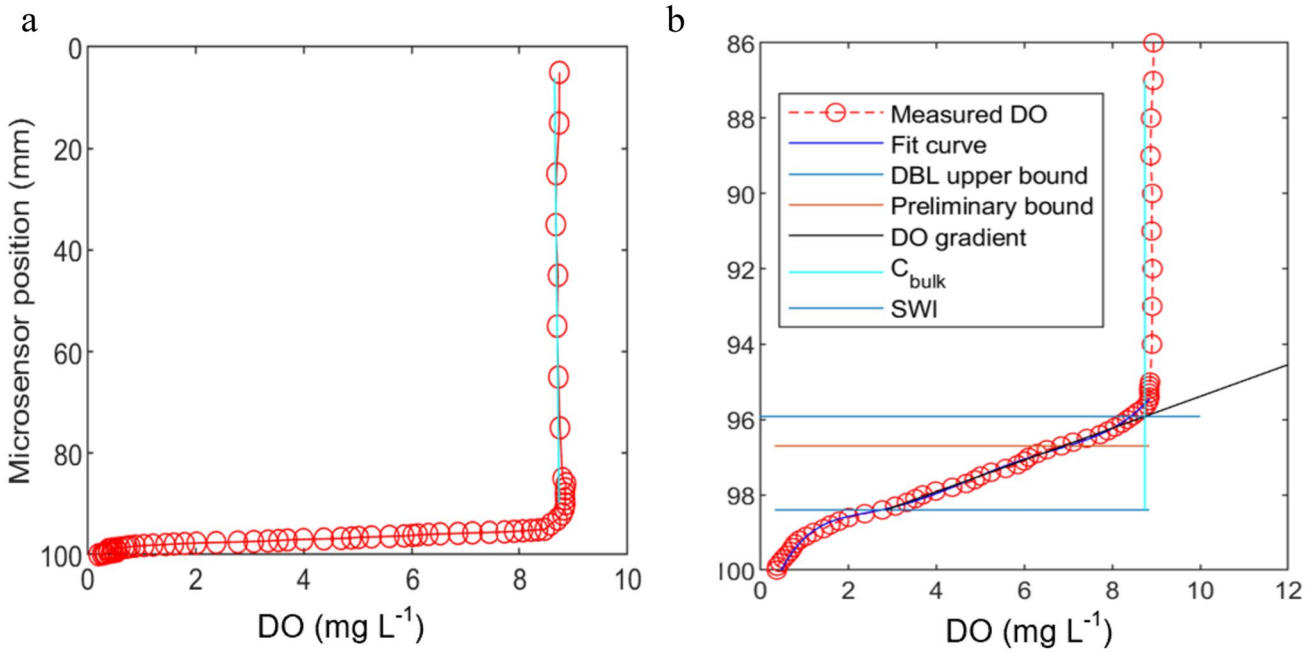

Fig. 3 A typical profile and the diffusive boundary layer (DBL) determined by the computational procedure. Y-axis indicates the downward distance the sensor traveled from the start of the profile. **a** The whole profile. **b** The part of profile closer to the sediment–water interface (SWI)

2.5 DBL and J_{O_2} modeling

In the modeling approach described here, δ_{DBL} is determined by Eq. (1) (Brand et al. 2009):

$$\delta_{DBL} = \left(\frac{C_{bulk}}{C_{swi}} - 1\right)\frac{D_w}{\sqrt{k_1 D_s}} \quad (1)$$

where C_{bulk} is the DO concentration in bulk water, C_{swi} is the DO concentration at the SWI, k_1 is the first-order kinetic rate constant (day^{-1}), and D_s is the diffusion coefficient of oxygen in the sediment ($D_s = \varnothing D_w$, where $\varnothing$ is the porosity). k_1 considers all the chemical/biological reactions in the upper sediment and assumes the lumped-up reaction has first-order kinetic. $\varnothing$ is obtained by analyzing the sediment at 0 ~ 1 cm depth from SWI (Azcue et al. 1997) after the microprofiler measurement for the FCR core and from the literature value for CCR/LH (Bierlein et al. 2017). k_1 is obtained by fitting a wide range of kinetic rate constants to first-order kinetic models (refer to Man et al. 2020). The best-fit k_1 value is the one that minimizes the root-mean square error (RMSE) of modeled DO profiles.

To simplify the model, for modeled profiles at each study site, C_{bulk} is set to the average measured C_{bulk} value. In addition, the transition from the bulk water to the DBL via the viscous sublayer is not considered. Instead, the DO concentration is assumed constant above the elevation of the modeled δ_{DBL} and decreases linearly from C_{bulk} at the upper bound of the modeled δ_{DBL} to C_{swi} at the SWI. Below the SWI, DO is transported by molecular diffusion and consumed by kinetic reaction and the upward reduced species fluxes (Man et al. 2020). The reduced species flux in FCR is estimated by sediment sample analysis based on the linear relationship between the total organic carbon mass accumulation rate (TOC-MAR) and the reduced flux (Steinsberger et al. 2017). The total organic carbon mass accumulation rate is calculated by Eq. (2):

$$\text{TOC-MAR} = SR \times \rho_{dry} \times (1 - \varnothing) \times TOC \times 10 \quad (2)$$

where TOC is the sediment organic matter (mg g^{-1}), SR is the literature sedimentation rate (0.1 cm year^{-1}) (Gray et al. 2009), and ρ_{dry} is the density of the sediment (g cm^{-3}, obtained after evaporating water at 110 °C) (Azcue et al. 1997). TOC was estimated as the loss of weight after heating the dried sediment sample to ~ 400 °C for 24 h (Schumacher 2002). $\varnothing$ is calculated by Eq. (3):

$$\varnothing(\%) = 100 - \frac{\rho_{Bulk}}{\rho_{dry}} \times 100 \quad (3)$$

where ρ_{Bulk} is the density of the sediment before evaporating water (g cm^{-3}). Due to the lack of sediment characteristic data, literature values of reduced species flux are adopted for CCR and LH (Steinsberger et al. 2020). The literature sedimentation rate is a sedimentation rate value from *RESSED – an online reservoir sedimentation survey database for the United States* (Gray et al. 2009). The sedimentation rate in FCR is not available in the database, so the value for a reservoir near Roanoke was adopted.

2.6 Validate the computational procedure using modeled profiles

The modeled DO profiles (refer to the above section) are used to validate the performance of the computational procedure. The evaluation addresses the practical problem that the "correct" SWI and DBL upper boundary positions are unknown for measured profiles. Brand et al.'s (2009) model was adopted to generate more realistic DO profiles rather than setting arbitrary or random δ_{DBL}. The modeled profiles are presented in the supplementary information (Fig. S2) for the readers' information, but the mechanism/quality of the model is beyond the scope of this manuscript.

3 Results and discussion

3.1 SWI and DBL characterized by the computational procedure

In Fig. 4, the computational (blue dots) and visual SWI positions determined by two independent inspectors (brown square for inspector 1; red triangle for inspector 2) are shown.

The methodology of the visual inspection method attempts to identify a linear part in the DO profile as the DBL (i.e., where $\frac{dDO}{dx}$ is a constant and $\frac{d^2DO}{dx^2}$ is zero). The methodology is simple and reflects the physics of the DBL, where molecular diffusion dominates. However, a plot of $\frac{dDO}{dx}$ and $\frac{d^2DO}{dx^2}$ of a typical profile presented in supplementary information (Fig. S1) does not show clear signal of DBL or SWI, which indicates the visual inspection method may not be reliable for real-world DO profiles.

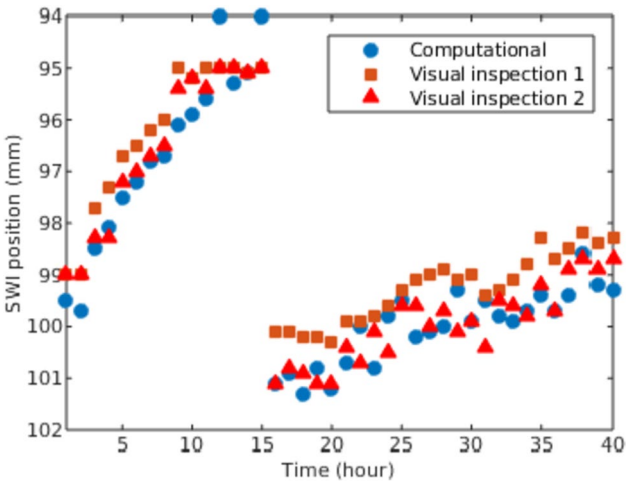

Fig. 4 The computational and visual sediment–water interfaces (SWI) (from two inspectors) in Lake Hallwil. The discontinuity of data at 15 h is due to the required repositioning of the microsensor to prevent it from shifting out of the measurement range as the base of the microprofiler slowly settled into the soft sediment. Sediment–water interface positions are relative to the lander's initial position (lander position 0 mm) with downward being positive

According to the observations of the data presented in Fig. 4, the SWI positions indicate a sinking microprofiler, and the sinking rate is decreasing smoothly during each deployment period. The minor fluctuation of the SWI positions is probably due to the noise in the DO signal and the non-steady character of the DO profiles. It supports the use of our computational procedure for characterizing the DBL and SWI given that our procedure is applicable to non-steady DO profiles.

The two inspectors are two co-authors of this paper who are both experienced in visually inspecting sediment DO profiles. Although very similar results are obtained independently, the two inspectors gave slightly different visually characterized SWIs, which is dependent on the inspector's subjective judgment. In contrast, the computationally characterized SWI is objective. To ensure consistency, the visual inspection results presented below are all based on visual inspection 2.

The comparison between the computational and visual SWIs at all three study sites is provided in Fig. 5. The computational SWI is generally close to the visual one, with the average variation between them in each water body in the range of 0.4–0.8 mm. The corresponding variation in DO flux can be up to 10.8 mmol m^2 day^{-1} estimated by simple film theory, while the DO flux in FCR measured by a sediment chamber was 14.0 ± 3.2 mmol m^2 day^{-1} (Krueger et al. 2020). The computational SWI for CCR and LH shows the same trend as the visual one, with the SWI position becoming closer to the microprofiler zero position. This trend is due to the unavoidable downward movement of the microprofiler when it is left at the bottom of the lake. This downward settling was corrected daily in CCR/LH (i.e., in situ studies) to prevent the microsensor from shifting out of the microprofiler measurement range. The corrections are visible in the gaps between data (e.g., at 20 h and 60 h in Fig. 5b). In FCR, the microprofiler was also repositioned once or twice per day for the same purpose as the in situ deployments. The microprofiler was not deployed at night in FCR (core) due to the limitation of battery capacity, which leads to the blanks between the profiles of two consecutive days (e.g., between 8 and 22 h in Fig. 5a). Compared to the amount of time required by the visual inspection method (usually days for hundreds of profiles), the computational method characterizes SWI automatically within a few seconds with equivalent accuracy. Referring to the testing results using modeled profiles of the computational procedure to be presented in Assessment section (Table 4), it appears that the average difference between the visual and computational SWI (0.4–0.8 mm in the three study sites) is much larger than the average difference between the computational and

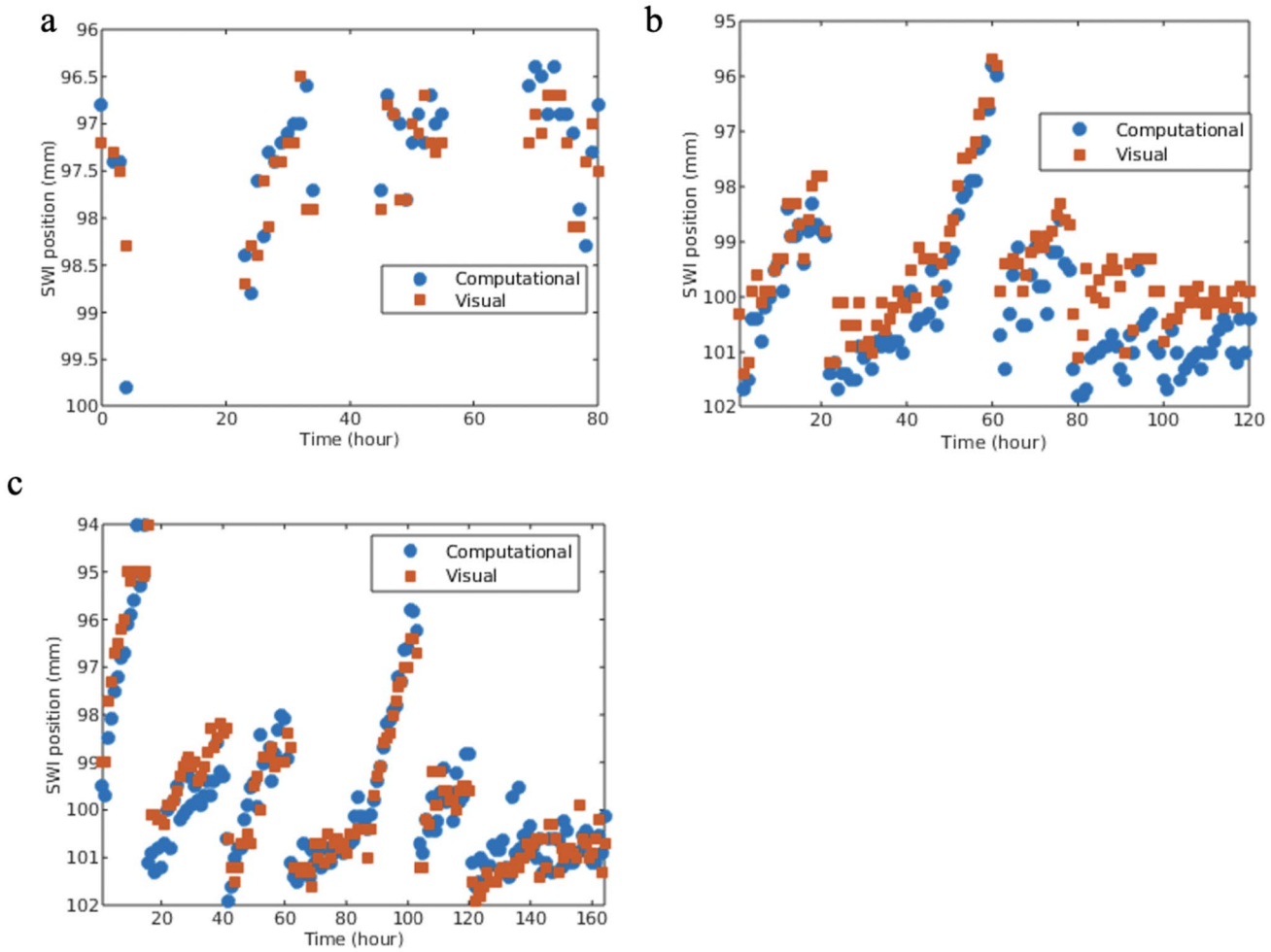

Fig. 5 The computational and visual characterized sediment–water interface (SWI) for the three study sites: **a** Falling Creek Reservoir (core), **b** Carvins Cove Reservoir, and **c** Lake Hallwil. In Falling Creek Reservoir (core), the microprofiler was not deployed at night

known SWI (0.1–0.3 mm), which supports adopting the described computational procedure.

Figure 6 presents four sample profiles at different aeration rates in FCR (core). It can be observed by visual inspection that for all four DO profiles presented here the computational procedure reasonably identifies the SWI (i.e., the DBL lower bounds). In these profiles, the DO concentration gradient is approximately constant above the computationally determined SWI and the DO concentration gradient becomes non-linear and smaller below the SWI than that in the DBL, which reflects the dominant DO diffusion process above the SWI and the complex DO consumption processes below the SWI, respectively.

Regarding the DBL upper bound, the final upper bound determined by the proposed procedure appears to be more accurate than the preliminary one. The final upper bounds are located at the transition region between the bulk water and the diffusion dominated region, but the preliminary upper bounds are still in the diffusion dominated regions in the DO profiles presented in Fig. 6b and d. To conclude, for most of the DO profiles under consideration, the proposed computational procedure correctly identifies the DBL as the part of the DO profile where the gradient is approximately constant.

Although similar results may be obtained by visual inspection and the computational procedure, the latter approach ensures that all DO profiles are obtained consistently and efficiently. It should be noted that this computational procedure does not yield perfect results for all DO profiles due to the ambiguity of the DBL upper and lower bounds. Effort has been made to avoid any subjective judgment in the computational procedure. For future applications, visual inspection may be adopted to guide the computational procedure for individual profiles that clearly deviate from the norm, especially for anoxic profiles where the DBL is more ambiguous than oxic profiles and the profiles whose fitted curves have low R^2 values.

Table 3 compares the computational and visual average δ_{DBL} at the three study sites. The computational δ_{DBL}

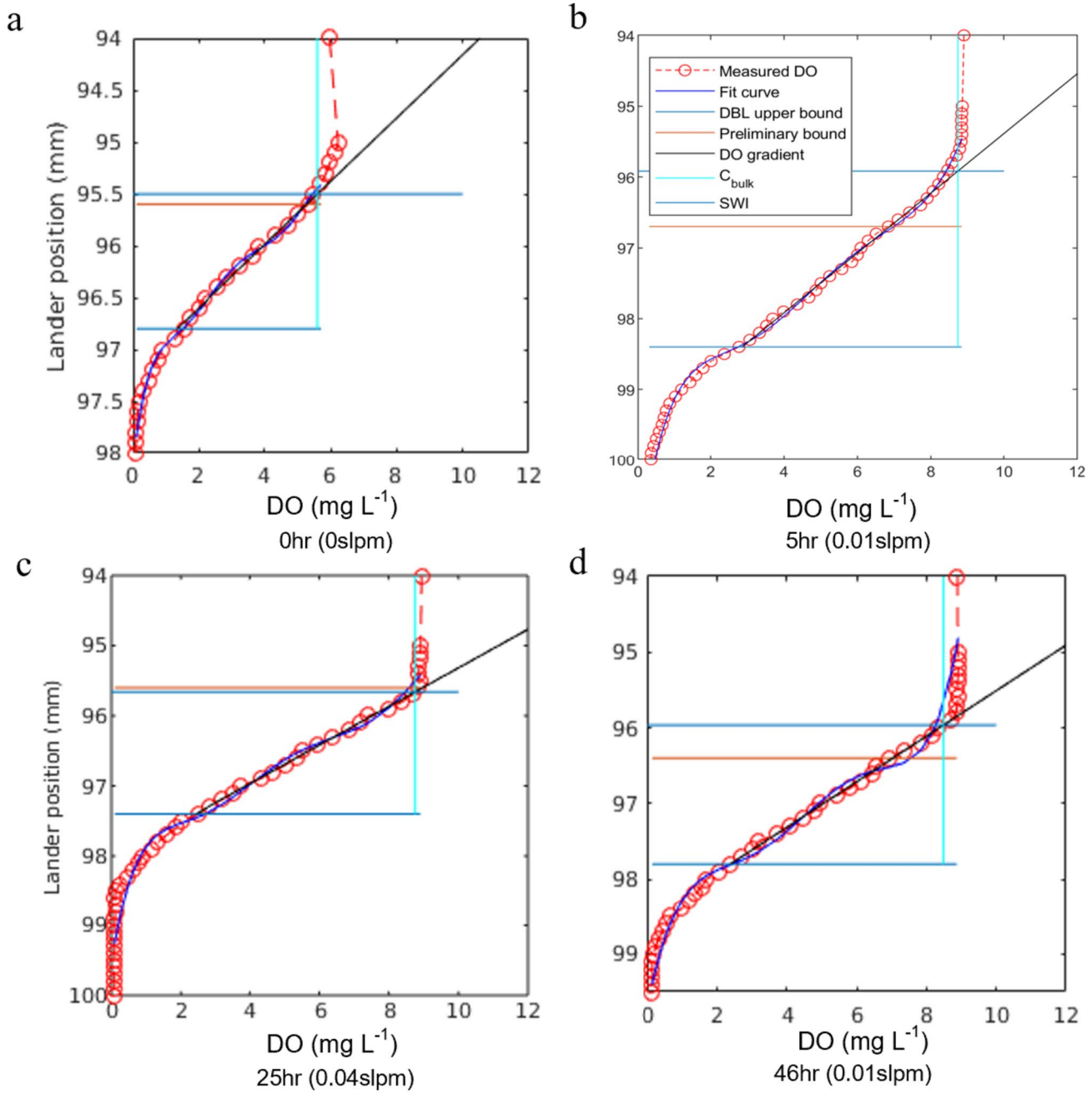

Fig. 6 Four typical profiles and the diffusive boundary layer (BDL) determined by the computational procedure in Falling Creek Reservoir. Measurement time and aeration rates are noted below each profile

Table 3 The date, number of profiles, and average computational and visual δ_{DBL} with one standard deviation in Falling Creek Reservoir, Carvins Cove Reservoir, and Lake Hallwil

Water body	Number of profiles	Date	Visual average δ_{DBL} (mm)	Computational average δ_{DBL} (mm)
FCR	38	2020 Nov 10–13	1.3 ± 1.7	1.5 ± 0.9
CCR	120	2013 May 26–June 01	0.9 ± 0.9	1.5 ± 0.9
LH	162	2012 May 24–June 01	1.3 ± 1.1	1.4 ± 0.6

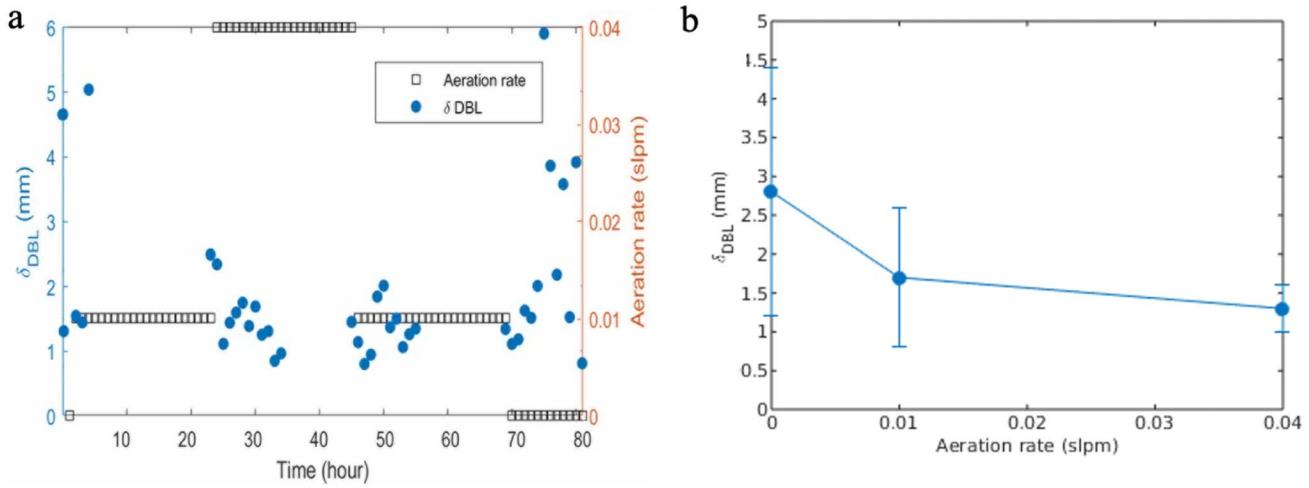

Fig. 7 **a** Computationally characterized δ_{DBL} and aeration rates in Falling Creek Reservoir. **b** average δ_{DBL} at each aeration rate in Falling Creek Reservoir

has lower standard deviations than the visual δ_{DBL} for LH and FCR. For CCR, although the two methods have equal standard deviation, the computational δ_{DBL} still yields more stable results since it has a larger average δ_{DBL} than the visual method (i.e., has lower coefficient of variation). Based on the discussion above, the computational δ_{DBL} is adopted in sections below for further analysis.

δ_{DBL} and aeration/oxygenation rate.

Figures 7, 8, and 9 present the relationship between δ_{DBL} and aeration/oxygenation rates in FCR, CCR, and LH, respectively. Subplots (a) provide the δ_{DBL} and aeration/oxygenation rate for all profiles, and subplots (b) provide the average δ_{DBL} at each aeration/oxygenation rate.

In the FCR sediment core, δ_{DBL} responds as expected to the aeration rate changes, with the higher aeration rates corresponding to smaller δ_{DBL}. In Fig. 7a, most δ_{DBL} less than 2 mm correspond to the high aeration rate (0.04 slpm) and the average δ_{DBL} in Fig. 7b has a clear negative relationship with the aeration rate.

In CCR, there is also a general correlation between δ_{DBL} and oxygenation rate. In Fig. 8a, most profiles have a δ_{DBL} less than 2 mm at high oxygenation rates (equal to or more than 473 slpm) and some profiles have a δ_{DBL} more than 4 mm at low oxygenation rates (less than 473 slpm). When the oxygenation rate is equal to or lower than 473 slpm, the average δ_{DBL} results in Fig. 8b suggest a negative relationship with the oxygenation rate. When the oxygenation rate is higher than 473 slpm, increasing aeration rate does not necessarily reduce δ_{DBL}.

In LH, a negative relationship of δ_{DBL} with the aeration rate change is also observed (Fig. 9). When the diffusers are

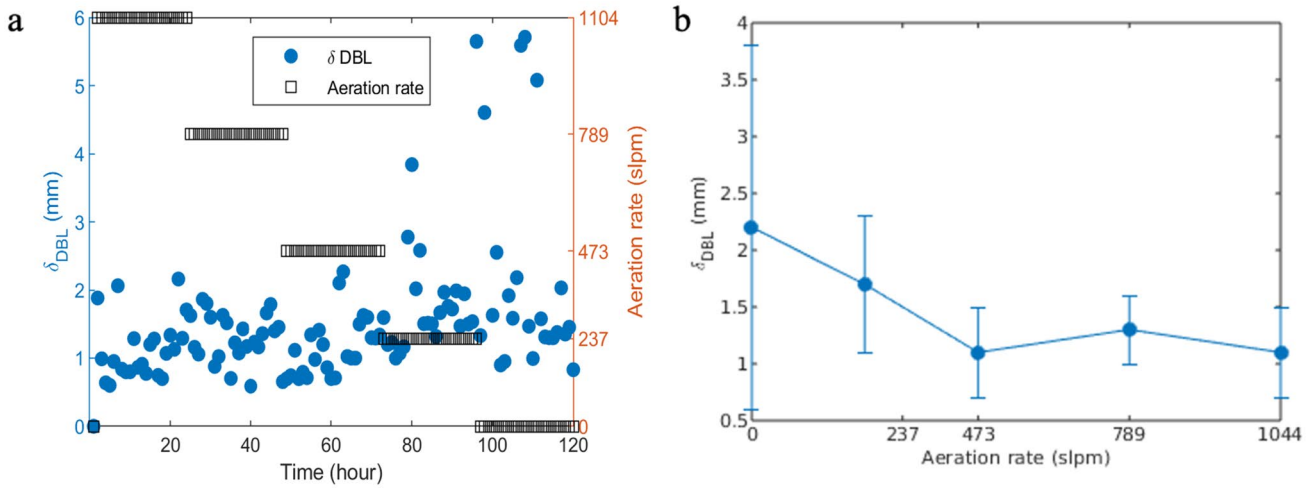

Fig. 8 **a** Computationally characterized δ_{DBL} and aeration rates in Carvins Cove Reservoir. **b** average δ_{DBL} at each aeration rate in Carvins Cove Reservoir

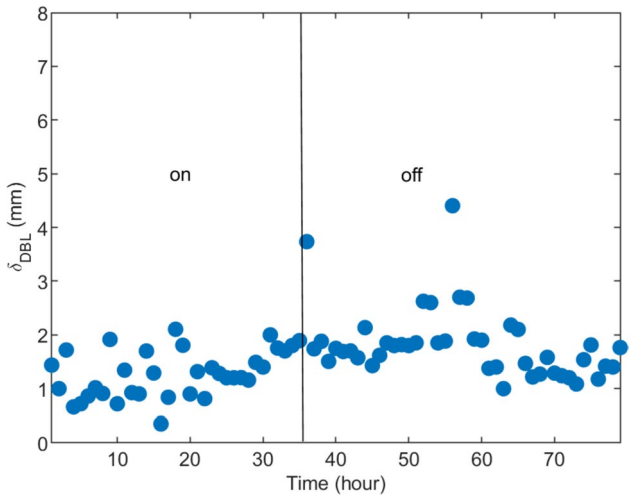

Fig. 9 Computationally characterized δ_{DBL} for bubble plume diffusers on and off in Lake Hallwil presented in time sequence. The microprofiler was 30 m from the diffusers

turned off, there is a distinct increase in δ_{DBL}, and the average δ_{DBL} increases from 1.4 to 1.8 mm. In Fig. 9, the aeration rate is not presented because there are only two conditions: "aeration on" and "aeration off." The aeration rate has been presented in Table 2, which is 2838 slpm. It should be noted that the experimental setup in LH adjusted both the oxygenation rate and the distance from the microprofiler to the diffusers, but the δ_{DBL} results with the microprofiler placed at 300 m and 3700 m from the diffusers are not presented here. The reason is that the diffusers were turned on all the time for the two distances and thus no comparison between diffusers on and diffusers off can be made. Furthermore, Wang et al. (2023) suggest bubble plume diffusers only impact near-field BBL turbulence structure.

To conclude, δ_{DBL} results from all three study sites appear reasonable by referring to field studies linking small δ_{DBL} to high turbulence dissipation rates in the BBL (Lorke et al. 2003; Bryant et al. 2010). The enhanced oxygenation may also lead to a thin DBL given that the hypolimnetic oxygenation/aeration systems have proved efficient in adding DO to the hypolimnion (Chen et al. 2018).

Table 4 Variations of the diffusive boundary layer upper and lower bound positions between the computational and known values for the modeled profiles, with one standard deviation

Water body	FCR	CCR	LH
Average difference of the DBL upper bounds (mm)	0 ± 0	0 ± 0	0 ± 0
Average difference of the DBL lower bounds (i.e., SWI) (mm)	0.1 ± 0.2	0.2 ± 0.2	0.3 ± 0.3

3.2 Verify the computational procedure with modeled profiles

Figure S1 presents several typical laboratory and modeled DO profiles for FCR sediment. In this section, the computational procedure was applied to the modeled DO profiles to further evaluate its performance. Table 4 presents the average variations of the DBL upper and lower bound positions between the computational determined and known values for the modeled DO profiles in the three study sites. As discussed in the Assessment section, the computational procedure determines the upper and lower DBL bounds successfully. The average difference in FCR is the least among the three study sites, supporting that the laboratory condition is better controlled than in situ. Another interesting point is that the DBL upper bounds are determined with zero difference from the known values. This finding supports using all the data points between two preliminary bounds for a linear regression for the purpose of obtaining the DO gradient in DBL, rather than adopting several data points near the SWI as existing studies usually do.

4 Conclusions

Current J_{O_2} predictions in stratified water bodies are empirical rather than mechanistic. Determining the DBL is essential for sediment and DBL modeling studies to predict J_{O_2} in a mechanistic way. However, both the upper and lower bounds of the DBL can be ambiguous especially for permeable sediments and at high turbulence. In this study, a computational procedure is introduced to determine the SWI and the DBL objectively and automatically. More than 300 DO profiles obtained in laboratory and in situ from three study sites with different aeration/oxygenation rates are examined. With a microprofiler, the laboratory experiment was able to replicate the DBL similar to field conditions. The proposed computational procedure can characterize the DBL well for sediment DO profiles in all three study sites under various turbulence-inducing oxygenation conditions and modeled DO profiles. This procedure can save time and improve consistency in determining DBL in future sediment/DBL modeling studies.

Supplementary Information The online version contains supplementary material available at https://doi.org/10.1007/s11368-024-03767-0.

Acknowledgements This research is partially supported by U.S. National Science Foundation (NSF) grant DEB-1753639 and the NSF graduate research fellowship to ASL (DGE-1651272). We thank Chunyi Wang for conducting the FCR sediment sample analysis, Heather Wander and Adrienne Breef-Pilz for help in collecting FCR sediment cores, and Michi Schurter, Arno Stöckli, and Christina Urbanczyk for help in CCR/LH field work.

Funding Open Access funding enabled and organized by CAUL and its Member Institutions National Science Foundation,DEB-1753639,Cayelan C. Carey

Data availability Code and data used for this study is available through https://doi.org/https://doi.org/10.5281/zenodo.5667027.

Declarations

Conflict of interest The authors declare no competing interests.

References

Archer D, Maier-Reimer E (1994) Effect of deep-sea sedimentary calcite preservation on atmospheric CO2 concentration. Nature 367:260–263. https://doi.org/10.1038/367260a0

Ashley KI (1985) Hypolimnetic aeration practical design and application. Water Res 19(6):735–740. https://doi.org/10.1016/0043-1354(85)90120-4

Azcue JM, Mudroch P, Mudroch A (1997) Manual of physico-chemical analysis of aquatic sediments. CRC Lewis

Berner RA, Canfield DE (1989) A new model for atmospheric oxygen over Phanerozoic time. Am J Sci 289:333–361. https://doi.org/10.2475/ajs.289.4.333

Beutel MW (2003) Hypolimnetic anoxia and sediment oxygen demand in California drinking water reservoirs. Lake Reserv Manage 19:208–221. https://doi.org/10.1080/07438140309354086

Bierlein KA, Rezvani M, Socolofsky SA, Bryant LD, Wüest A, Little JC (2017) Increased sediment oxygen flux in lakes and reservoirs: the impact of hypolimnetic oxygenation. Water Resour Res 53:4876–4890. https://doi.org/10.1002/2016WR019850

Bierlein KA (2015) Predicting induced sediment oxygen flux in oxygenated lakes and reservoirs. Unpublished PhD dissertation, Virginia Tech. Blacksburg, U.S. https://vtechworks.lib.vt.edu/handle/10919/73502

Birt D, Wain D, Slavin E, Zang J, Luckwell R, Bryant LD (2021) Stratification in a reservoir mixed by bubble plumes under future climate scenarios. Water 13. https://doi.org/10.3390/w13182467

Boudreau BP, Jørgensen BB (2001) The benthic boundary layer: transport processes and biogeochemistry. Oxford University Press

Brand A, Dinkel C, Wehrli B (2009) Influence of the diffusive boundary layer on solute dynamics in the sediments of a seiche-driven lake: a model study. J Geophys Res: Biogeosci 114. https://doi.org/10.1029/2008JG000755

Bryant LD, McGinnis DF, Lorrai C, Brand A, Little JC, Wüest A (2010) Evaluating oxygen fluxes using microprofiles from both sides of the sediment-water interface. Limnol Oceanogr: Meth 8:610–627. https://doi.org/10.4319/lom.2010.8.0610

Bryant LD, Gantzer PA, Little JC (2011a) Increased sediment oxygen uptake caused by oxygenation-induced hypolimnetic mixing. Water Res 45(3692):3703. https://doi.org/10.1016/j.watres.2011.04.018

Bryant LD, Hsu-Kim H, Gantzer PA, Little JC (2011b) Solving the problem at the source controlling Mn release at the sediment-water interface via hypolimnetic oxygenation. Water Res 45(19):6381–6392. https://doi.org/10.1016/j.watres.2011.09.030

Burris VL, McGinnis DF, Little JC (2002) Predicting oxygen transfer and water flow rate in airlift aerators. Water Res 36(18):4605–4615. https://doi.org/10.1016/S0043-1354(02)00176-8

Chen S, Lei C, Carey CC, Gantzer PA, Little JC (2017) A coupled three-dimensional hydrodynamic model for predicting hypolimnetic oxygenation and epilimnetic mixing in a shallow eutrophic reservoir. Water Resour Res 53(470):484. https://doi.org/10.1002/2016WR019279

Chen S, Little JC, Carey CC, McClure RP, Lofton ME, Lei C (2018) Three-dimensional effects of artificial mixing in a shallow drinking-water reservoir. Water Resour Res 54:425–441. https://doi.org/10.1002/2017WR021127

Doubek JP, Campbell KL, Doubek KM, Hamre KD, Lofton ME, McClure RP, Ward NK, Carey CC (2018) The effects of hypolimnetic anoxia on the diel vertical migration of freshwater crustacean zooplankton. Ecosphere 9:2332

Gantzer PA, Preece EP, Nine B, Morris J (2019) Decreased oxygenation demand following hypolimnetic oxygenation. Lake Reserv Manage 35:292–307. https://doi.org/10.1080/10402381.2019.1648614

Gantzer PA, Bryant LD, Little JC (2009) Effect of hypolimnetic oxygenation on oxygen depletion rates in two water-supply reservoirs. Water Res 43(6):1700–1710. https://doi.org/10.1016/j.watres.2008.12.053

Gerling AB, Browne RG, Gantzer PA, Mobley MH, Little JC, Carey CC (2014) First report of the successful operation of a side stream supersaturation hypolimnetic oxygenation system in a eutrophic shallow reservoir. Water Res 67(129):143. https://doi.org/10.1016/j.watres.2014.09.002

Glud RN (2008) Oxygen dynamics of marine sediments. Mar Biol Res 4:243–289. https://doi.org/10.1080/17451000801888726

Gray JR, Bernard JM, Stewart DW, Schwarz GE, Ray KT (2009) RESSED – an online reservoir sedimentation survey database for the United States National Interdisciplinary Conference. Soil & Water Conservation Society, Kansas City, Missouri

Hipsey MR, Bruce LC, Boon C, Busch B, Carey CC, Hamilton DP, Hanson PC, Read JS, de Sousa E, Weber M, Winslow LA (2019) A General Lake Model (GLM 3.0) for linking with high-frequency sensor data from the Global Lake Ecological Observatory Network (GLEON). Geosci Model Dev 12:473–523. https://doi.org/10.5194/gmd-12-473-2019

Hoffmann K, Bienhold C, Buttigieg PL, Knittel K, Laso-Pérez R, Rapp JZ, Boetius A, Offre P (2020) Diversity and metabolism of Woeseiales bacteria, global members of marine sediment communities. ISME J 14(4):1042–1056. https://doi.org/10.1038/s41396-020-0588-4

Holzner CP, Tomonaga Y, Stöckli A, Denecke N, Kipfer R (2012) Using noble gases to analyze the efficiency of artificial aeration in Lake Hallwil, Switzerland. Water Resour Res 48. https://doi.org/10.1029/2012WR012030

Jane SF et al (2021) Widespread deoxygenation of temperate lakes. Nature 594:66–70. https://doi.org/10.1038/s41586-021-03550-y

Jenny J-P, Francus P, Normandeau A, Lapointe F, Perga M-E, Ojala A, Schimmelmann A, Zolitschka B (2016) Global spread of hypoxia in freshwater ecosystems during the last three centuries is caused by rising local human pressure. Global Change Biol 22:1481–1489. https://doi.org/10.1111/gcb.13193

Jørgensen BB, Revsbech NP (1985) Diffusive boundary layers and the oxygen uptake of sediments and detritus. Limnol Oceanogr 1. https://doi.org/10.4319/lo.1985.30.1.0111

Krueger KM, Vavrus CE, Lofton ME, McClure RP, Gantzer P, Carey CC, Schreiber ME (2020) Iron and manganese fluxes across the sediment-water interface in a drinking water reservoir. Water Res 182:116003–116003. https://doi.org/10.1016/j.watres.2020.116003

Lorke A, Müller B, Maerki M, Wüest A (2003) Breathing sediments: the control of diffusive transport across the sediment—water interface by periodic boundary-layer turbulence. Limnol Oceanogr 48:2077–2085. https://doi.org/10.4319/lo.2003.48.6.2077

Man X, Bierlein KA, Lei C, Bryant LD, Wüest A, Little JC (2020) Improved modeling of sediment oxygen kinetics and fluxes in lakes and reservoirs. Environ Sci Tech 54:2658–2666. https://doi.org/10.1021/acs.est.9b04831

McGinnis DF, Little JC (2002) Predicting diffused-bubble oxygen transfer rate using the discrete-bubble model. Water Res 36(18):4627–4635. https://doi.org/10.1016/S0043-1354(02)00175-6

Moore BC, Chen PH, Funk WH, Yonge D (1996) A model for predicting lake sediment oxygen demand following hypolimnetic aeration. J Am Water Resour Assoc 32(4):723–731. https://doi.org/10.1111/j.1752-1688.1996.tb03469.x

Müller B, Bryant LD, Matzinger A, Wüest A (2012) Hypolimnetic oxygen depletion in eutrophic lakes. Environ Sci Tech 46:9964–9971. https://doi.org/10.1021/es301422r

Nürnberg GK (1987) A comparison of internal phosphorus loads in lakes with anoxic hypolimnia: laboratory incubation versus in situ hypolimnetic phosphorus accumulation1. Limnol Oceanogr 32:1160–1164. https://doi.org/10.4319/lo.1987.32.5.1160

Preece EP, Moore BC, Skinner MM, Child A, Dent S (2019) A review of the biological and chemical effects of hypolimnetic oxygenation. Lake Reserv Manage 35(3):229–246. https://doi.org/10.1080/10402381.2019.1580325

Rezvani M (2016) Bubble plumes in crossflow: laboratory and field measurements of their fluid dynamic properties with application to lake aeration and management. University, Texas A.M

Riedl RJ, Huang N, Machan R (1972) The subtidal pump: a mechanism of interstitial water exchange by wave action. Marine Bio 13:210–221. https://doi.org/10.1007/BF00391379

Schumacher B (2002) Methods for the determination of total organic carbon (TOC) in soils and sediments. Ecological Risk Assessment Support Center Office of Research and Development. U.S. Environmental Protection Agency, Cincinnati, OH, USA

Steinsberger T, Schmid M, Wüest A, Schwefel R, Wehrli B, Müller B (2017) Organic carbon mass accumulation rate regulates the flux of reduced substances from the sediments of deep lakes. Biogeosciences 14:3275–3285. https://doi.org/10.5194/bg-14-3275-2017

Steinsberger T, Schwefel R, Wüest A, Müller B (2020) Hypolimnetic oxygen depletion rates in deep lakes: effects of trophic state and organic matter accumulation. Limnol Oceanogr 65:3128–3138. https://doi.org/10.1002/lno.11578

The MathWorks Inc (2022) MATLAB version: 9.13.0 (R2022b), Natick, Massachusetts: The MathWorks Inc. https://www.mathworks.com

Wang B, Rezvani M, Bierlein KA, Bryant LD, Little JC, Wüest A, Socolofsky SA (2023) Effects of bubble plumes on lake dynamics, near-bottom turbulence, and transfer of dissolved oxygen at the sediment-water interface. Water Resour Res 59. https://doi.org/10.1029/2022WR032861

Zaw M, Chiswell B (1999) Iron and manganese dynamics in lake water. Water Res 33:1900–1910. https://doi.org/10.1016/S0043-1354(98)00360-1